


Multimethod approach to understand the assembly of cellulose fibrils in the biosynthesis of bacterial cellulose

Paavo A. Penttilä  · Tomoya Imai · Marie Capron · Masahiro Mizuno · Yoshihiko Amano · Ralf Schweins · Junji Sugiyama

Received: 22 December 2017 / Accepted: 12 March 2018 / Published online: 17 March 2018
© Springer Science+Business Media B.V., part of Springer Nature 2018

Abstract The production of controlled bacterial cellulose structures for various applications requires a better understanding on the mechanism of cellulose biosynthesis as well as proper tools for structural characterization of the materials. In this work, bacterial celluloses synthesized by an *Asaia bogorensis* strain known to produce fine cellulose fibrils and a commonly used *Komagataeibacter xylinus* strain were characterized using a comprehensive set of methods covering multiple levels of the hierarchical structure. FT-IR spectroscopy and x-ray diffraction were used to analyse the crystal structure and crystallite dimensions, whereas scanning and transmission electron microscopy, atomic force microscopy, and small-angle x-ray and neutron scattering were employed to

obtain information on the higher-level fibrillar structures. All methods yielded results consistent with the *A. bogorensis* cellulose fibrils being thinner than the *K. xylinus* fibrils on both the level of individual cellulose microfibrils and bundles or ribbons thereof, even though the exact values determined for the lateral fibril dimensions depended slightly on the method and sample preparation. Particularly, the width of microfibril bundles determined by the microscopy methods differed due to shrinkage and preferred orientation caused by drying, whereas the microfibril diameter remained unaffected. The results were used to understand the biological origin of the differences between the two bacterial celluloses.

Electronic supplementary material The online version of this article (<https://doi.org/10.1007/s10570-018-1755-x>) contains supplementary material, which is available to authorized users.

Keywords Bacterial cellulose · Structural characterization · Cellulose biosynthesis · Small-angle scattering

P. A. Penttilä (✉) · R. Schweins
Science Division/Large-Scale Structures Group, Institut
Laue–Langevin (ILL), 71 avenue des Martyrs,
38042 Grenoble, France
e-mail: paavo.a.penttila@alumni.helsinki.fi

M. Capron
Partnership for Soft Condensed Matter (PSCM), 71
avenue des Martyrs, 38043 Grenoble, France

P. A. Penttilä · T. Imai · J. Sugiyama
Research Institute for Sustainable Humanosphere (RISH),
Kyoto University, Gokasho, Uji 611-0011, Japan

M. Mizuno · Y. Amano
Institute of Engineering, Academic Assembly, Shinshu
University, Nagano 380-8553, Japan

M. Capron
ESRF – The European Synchrotron, 71 avenue des
Martyrs, 38043 Grenoble, France

Introduction

Cellulose produced by various types of bacteria has gained considerable attention due to applications in the fields of materials, medicine, and foods (Lin et al. 2013). The main benefits of bacterial cellulose (BC) include high purity, light and water-swollen structure, non-toxicity, and biodegradability. On the other hand, BC produced under special culturing conditions or in the presence of additives like hemicelluloses can be used to understand the cellulose biosynthesis, not only in bacteria but also in higher plants (Atalla et al. 1993; Penttilä et al. 2017; Tokoh et al. 2002a).

An additional advantage of BC over cellulose from plant sources is the potential to control the synthesized structures through genetic engineering with minimal interference of other components. Recent advances in the field of BC biosynthesis (McNamara et al. 2015) have led to a more complete understanding of the cellulose-producing machinery in bacteria, allowing more detailed interpretation of interlinks between genetic information and protein function as well as their relationship with the synthesized cellulose structures. An interesting system from this point of view is the *Asaia bogorensis* JCM 10569 substrain AJ, which was previously observed to produce especially fine cellulose fibrils (Kumagai et al. 2011), yet the reason for this is unclear and the precise dimensions of the microfibrils have so far not been reported.

In order to detect specific structural differences between BC samples, efficient and accurate methods to characterize their hierarchical structure are desired. With a wide range of methods appearing in the literature and the intrinsic differences between BC samples produced at different conditions, it is difficult to find comparable values describing for instance the cross-sectional dimensions of BC fibrils. Furthermore, most of the conventional techniques require drying of the sample before observation or allow only small details of the sample to be studied at a time, due to which the results might not necessarily reflect the true structure of the hydrated three-dimensional fibril network. An exception to this are small-angle scattering methods utilizing x-rays or neutrons, which allow measurements of macroscopic never-dried BC samples and simultaneous characterization of the fibrillar elements over multiple levels of structural hierarchy (Penttilä et al. 2017; Martínez-Sanz et al. 2015a).

This work aims at comparing the cross-sectional fibril dimensions of two distinct types of BC, determined by a comprehensive set of physical characterization methods extending from the molecular scale to the three-dimensional fibril network. The BCs under investigation were synthesized by a common *Acetobacter* strain and the less characterized *A. bogorensis* JCM 10569 substrain AJ (Kumagai et al. 2011). The molecular structure and crystal structure were studied with FT-IR spectroscopy and x-ray diffraction (XRD), and the structure of microfibril bundles with scanning and transmission electron microscopy (SEM and TEM) and atomic force microscopy (AFM), of which TEM and AFM allowed the identification of substructures inside of the bundles and AFM the distinction between bundle width and thickness. The whole lengthscale from BC microfibrils to the outer dimensions of the microfibril bundles in never-dried samples was covered by small-angle x-ray and neutron scattering (SAXS and SANS), where a single model was used to fit the data on both levels of the hierarchical structure simultaneously. The structural information accessible by the different methods will be critically discussed and compared to each other and to literature values. The results will also be interpreted from the perspective of cellulose biosynthesis and used to elucidate the causes of the structural differences between the two BCs.

Experimental

Preparation of BC samples

Asaia bogorensis JCM 10569 substrain AJ (Kumagai et al. 2011) was cultured in 5-L conical flasks containing 1 L of Schramm–Hestrin (SH) medium. After incubating for 7 days at 25°C, a white film or pellicle was formed on the surface of the medium or it had sunk into the solution. The cellulosic product together with the bacteria was collected by centrifugation and washed by adapting the procedures from Kumagai et al. (2011): first treated with 2% NaOH at 100°C for 1 h, then purified by soaking in a mixture of 0.34% NaClO₂, 0.54% NaOH, and 1.5% (v/v) CH₃COOH at 70°C for 2 h, and finally suspended in a solution containing 1 mg/ml Proteinase K (Wako), 0.1% (w/w) SDS, and 0.01 M Tris–HCl buffer (pH 8.0 at 4°C) at 50°C for 24 h. The product was thoroughly

washed by centrifuging with water after each step and stored at 4°C. For comparison, *Komagataeibacter xylinus* (ATCC 53524, formerly known as *Gluconacetobacter xylinus*) was incubated in 20 ml of SH medium in a 100-ml conical flask at 28°C for 4 days and the resulting cellulose pellicle was washed similarly to the *A. bogorensis* cellulose, but using magnetic stirring in water instead of centrifugation.

FT-IR spectroscopy

Freeze-dried samples were pressed on the attenuated total reflectance crystal of a Perkin Elmer Frontier FT-IR spectrometer. For at least two specimens from each BC sample, 16 scans on spectral range from 400 to 4000 cm⁻¹ with 4 cm⁻¹ resolution were collected and averaged after baseline-correction, subtraction of constant background (signal around 1800 cm⁻¹), and normalization to signal at 1110 cm⁻¹.

X-ray diffraction

Approximately 2 mg of purified and freeze-dried BC was immersed in 100 µl water for about 2 h, then placed on a glass microscope slide, pressed flat with another glass slide, and allowed to dry at room temperature for 2–3 days. In such way, the BC fibrils were expected to orient randomly in a plane parallel to the glass slide surface, thus enhancing the diffraction peaks with Miller indices *hk0* when measured in reflection mode. XRD was measured in symmetric reflection mode with a θ - 2θ diffractometer and scintillation counter, using Cu-K α radiation (wavelength $\lambda = 1.54$ Å) produced by a Rigaku Ultrax 18HB x-ray generator operated at 40 kV voltage and 300 mA current. In total 2 to 3 scans per sample were collected between scattering angles $2\theta = 5^\circ$ and 40° with a step size of 0.05° and scan rate of $1^\circ/\text{min}$.

The crystal dimensions were calculated using the Scherrer equation

$$L_{hkl} = \frac{K\lambda}{\beta_{hkl} \cos \theta_{hkl}}, \quad (1)$$

where K is the Scherrer constant (here chosen as $K = 1$), β_{hkl} the integral breadth, and θ_{hkl} the Bragg angle of reflection *hkl*. XRD intensities in the range $2\theta = 11^\circ$ to 26° were fitted with four pseudo-Voigt functions (sum of Gaussian and Lorentzian functions

centered at the same position), three of them corresponding to the strongest reflections of cellulose I_α/I_β (100/1-10, 010/110, and 110/200 (Nishiyama et al. 2002; Nishiyama et al. 2003)) and the fourth approximating mostly the scattering from the glass slide as well as some less-ordered cellulose and the other cellulose reflections. An instrumental broadening of $\beta_{inst} = 0.19^\circ$ around $2\theta = 18^\circ$ was determined by measuring hexamethylenetetramine ((CH₂)₆N₄) powder attached to a glass slide and used to correct the measured values of peak width ($\beta_{hkl,m}$):

$$\beta_{hkl}^2 = \beta_{hkl,m}^2 - \beta_{inst}^2.$$

Scanning electron microscopy

Freeze-dried pieces of BC were placed on double-sided conductive tape and coated with platinum (JEOL JFC-1600; 10 mA, 90 s). Field-emission SEM imaging was done with a JEOL JSM-7800F Prime microscope with operation voltage 1.5 kV and using the lower secondary electron detector. Fibril widths were analysed from images obtained at 120,000-times magnification, using the measuring tool of ImageJ software (Schneider et al. 2012). Altogether 1877 fibril widths in 67 images with *A. bogorensis* cellulose and 721 fibril widths in 35 images with *K. xylinus* cellulose were included in the analysis.

Transmission electron microscopy

Samples used for XRD analysis were reimmersed in water and sonicated for 20 min in an ultrasonic bath (Yamato Branson 5210) to disperse the fibrils. After sonication, pieces of BC were deposited on glow-discharged, carbon-coated copper meshes and negatively stained by 2% uranyl acetate. The samples were imaged with a JEOL JEM-2000EXII electron microscope operated at 100 kV and equipped with a MegaViewG2 CCD camera (Olympus Soft Imaging Solutions). The widths of BC fibrils in images taken at 150,000-times magnification were measured using ImageJ, similarly to the SEM images.

Atomic force microscopy

Pieces of washed BC were placed on flat mica surfaces and allowed to dry for several days in a desiccator under N₂ flow. AFM imaging was done at ambient

conditions using an Asylum Research MFP-3D microscope equipped with a high-resolution tip (Bruker MSNL-10; radius 2 nm, spring constant 0.6 N/m) in tapping mode. The analysis of the AFM images was carried out using the Gwyddion 2.48 software (<http://gwyddion.net/>). Plane leveling and alignment of rows were done as corrections to the raw data. The widths of the BC fibrils were determined from $2.0\mu\text{m} \times 2.0\mu\text{m}$ amplitude images for *K. xylinus* cellulose and from $0.5\mu\text{m} \times 0.5\mu\text{m}$ amplitude images for *A. bogorensis* cellulose.

Small-angle x-ray and neutron scattering

SAXS was measured at the D2am beamline of the European Synchrotron Radiation Facility (ESRF) using an x-ray beam with wavelength $\lambda = 0.69 \text{ \AA}$ and an XPAD-D5 hybrid pixel detector. A piece of washed BC in H_2O was placed inside a glass capillary with 3-mm diameter and measured at several spots. The SAXS patterns were normalized by the reading of a photomultiplier situated downstream of the sample, corrected for solid angle, and integrated azimuthally using the pyFAI (Ashiotis et al. 2015) and FabIO (Knudsen et al. 2013) Python packages. The integrated intensities from patterns measured at different spots were averaged and a background intensity (pure H_2O) was subtracted. The data were binned and error bars for the intensity were generated using SASfit (Breßler et al. 2015).

SANS measurements (Penttilä and Schweins 2017) were carried out at the D11 instrument of the Institut Laue–Langevin (ILL) using sample-to-detector distances of 1.5 m, 8 m, and 34 m for a neutron wavelength of $\lambda = 6 \text{ \AA}$ and 34 m for $\lambda = 13 \text{ \AA}$, with the wavelength resolution being $\Delta\lambda/\lambda = 0.09$. The H_2O solution of the washed BC was replaced by D_2O and the samples were measured inside of quartz glass cells with 1 mm optical path. Corrections to SANS data, azimuthal integration, and merging of data from different detector positions were done using LAMP, the Large Array Manipulation Program (http://www.ill.eu/data_treat/lamp/the-lamp-book/).

Fitting of all small-angle scattering data was done in SasView (<http://www.sasview.org/>) using the unified exponential/power-law model (Beaucage 1995, 1996) with maximum three levels of hierarchy ($i = 1, 2, 3$ in increasing order of structure size):

$$I(q) = G_1 \exp\left(-\frac{q^2 R_{g,1}^2}{3}\right) + B_1 \left(\frac{[\text{erf}(qR_{g,1}/\sqrt{6})]^3}{q}\right)^{P_1} + G_2 \exp\left(-\frac{q^2 R_{g,2}^2}{3}\right) + B_2 \exp\left(-\frac{q^2 R_{g,1}^2}{3}\right) \times \left(\frac{[\text{erf}(qR_{g,2}/\sqrt{6})]^3}{q}\right)^{P_2} + B_3 \exp\left(-\frac{q^2 R_{g,2}^2}{3}\right) \frac{1}{q^{P_3}} + C \quad (2)$$

In Eq. 2, $R_{g,i}$ is the radius of gyration of particles at structural level i , P_i is the power-law exponent corresponding to their inner/surface structure, and G_i , B_i , and C are constants. The power-law exponent P_1 was fixed to 4 in all fits based on previously analyzed SAXS data using the same model (Penttilä et al. 2017). The magnitude of the scattering vector is defined as $q = 4\pi \sin \theta/\lambda$ with scattering angle 2θ .

Results and discussion

FT-IR spectroscopy results

The FT-IR spectra of BC samples produced by *K. xylinus* and *A. bogorensis* are presented in Fig. 1. The absorption bands characteristic of cellulose crystalline allomorphs I_α ($750, 3240 \text{ cm}^{-1}$) and I_β ($710, 3270 \text{ cm}^{-1}$) (Sugiyama et al. 1991) could all be clearly observed in *K. xylinus* cellulose, whereas in *A. bogorensis* cellulose the I_α signals were either very weak or completely absent (inset in Fig. 1). A comparison of signals at 710 and 750 cm^{-1} , done by fitting two Gaussian functions on top of a polynomial background and computing the peak areas, yielded apparent cellulose I_α fractions of 0.50 ± 0.02 and 0.04 ± 0.05 for *K. xylinus* and *A. bogorensis* celluloses, respectively. Here the error estimate is equal to the standard deviation of results from several specimens or different batches. Therefore, the current data confirmed qualitatively the previously reported higher I_β proportion of *A. bogorensis* cellulose (Kumagai et al. 2011).

In the OH and CH stretching regions of the FT-IR spectra, around $3000\text{--}3600$ and $2800\text{--}3000 \text{ cm}^{-1}$, respectively, broader peaks were observed for the *A.*

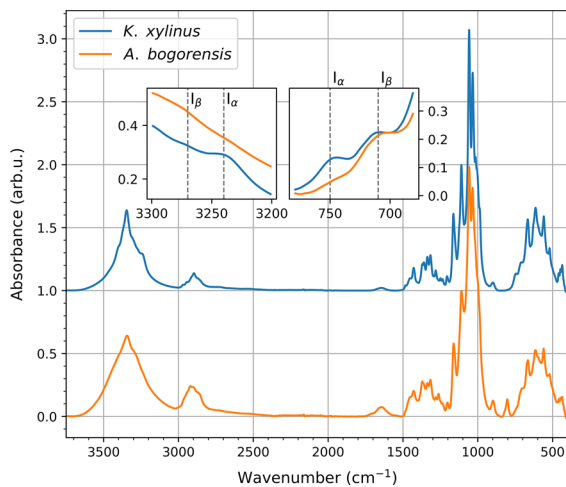


Fig. 1 FTIR spectra of BC samples, with the inset showing enlarged the characteristic absorption bands of cellulose I_α and I_β

bogorensis cellulose than for *K. xylinus* cellulose (Fig. 1). This was probably caused by the overall lower crystallinity or smaller crystal size of the *A. bogorensis* cellulose, as previously reported based on CP/MAS ^{13}C NMR spectra (Kumagai et al. 2011).

X-ray diffraction results

The XRD intensities together with fits used to calculate the crystal dimensions are presented in Fig. 2. The obtained lattice spacings (d_{hkl}) and crystal dimensions (L_{hkl}) are reported in Table 1, where the error estimates are based on two measurements and fits. The broader peaks in *A. bogorensis* cellulose (Fig. 2b) as compared to *K. xylinus* cellulose (Fig. 2a) indicated smaller lateral crystal dimensions in *A. bogorensis* cellulose, which was confirmed by the values calculated based on the fits (Table 1). The lateral crystal dimensions obtained for *K. xylinus* cellulose are in agreement with values 5–9 nm typically reported for pure bacterial celluloses (Klemm et al. 2005; Martínez-Sanz et al. 2015b; Fang and Catchmark 2014), and they were 1.3–1.6 times larger than those obtained for *A. bogorensis* cellulose. The current data provides the first direct evidence for the smaller crystal size of *A. bogorensis* cellulose, which was suggested by Kumagai et al. (2011) based on CP/MAS ^{13}C NMR spectra.

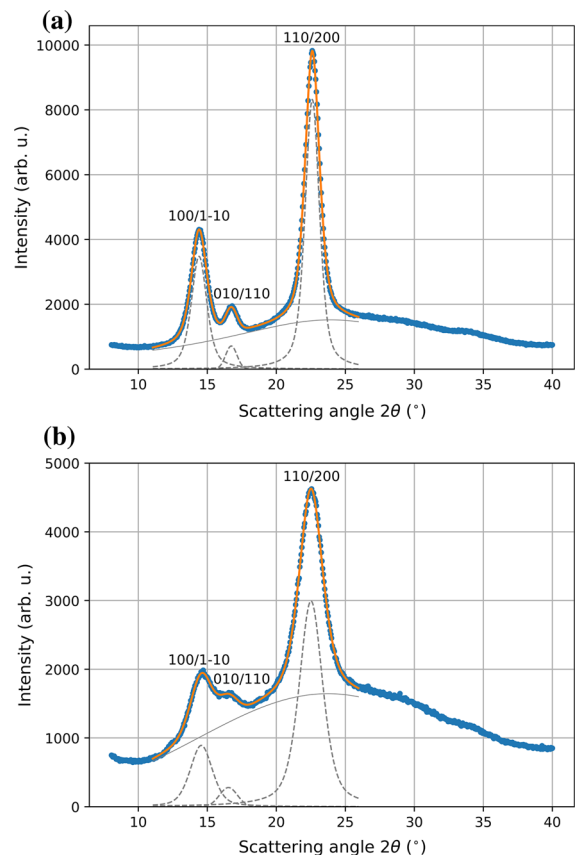


Fig. 2 XRD intensities (points) of cellulose produced by **a** *K. xylinus* and **b** *A. bogorensis*, shown together with the total fit (thick continuous line) and its components (dashed line for diffraction peaks and thin continuous line for background)

The lattice spacings of *K. xylinus* cellulose were similar to those reported for *Acetobacter* cellulose in general (Fang and Catchmark 2014; Iwata et al. 1998; Tokoh et al. 2002b). In *A. bogorensis* cellulose, the value of $d_{100/1-10}$ was slightly lower and $d_{010/110}$ higher than in *K. xylinus* cellulose, which is in agreement with the higher cellulose I_β content of the *A. bogorensis* cellulose. A similar shift has been observed together with a decrease of crystal size and increase of cellulose I_β proportion for BC produced in the presence of hemicelluloses (Iwata et al. 1998; Tokoh et al. 2002b).

Scanning electron microscopy results

Examples of SEM images and the distributions of fibril width based on an analysis of a large number of images are shown in Fig. 3. Additional SEM images

Table 1 Lattice spacings (d_{hkl}) and crystal dimensions (L_{hkl}) obtained from XRD fits (in nm)

Bacterium	$d_{100/1-10}$	$L_{100/1-10}$	$d_{010/110}$	$L_{010/110}$	$d_{110/200}$	$L_{110/200}$
<i>K. xylinus</i>	0.6141(3)	4.99(3)	0.5290(2)	8.9(2)	0.3928(1)	5.52(4)
<i>A. bogorensis</i>	0.6074(8)	3.71(9)	0.5356(7)	5.54(2)	0.3945(2)	3.36(2)

can be found in the Electronic supplementary material (Figure S1). The mean widths of *K. xylinus* and *A. bogorensis* cellulose fibrils were 33 ± 12 and 21 ± 6 nm, respectively, where the error estimate is equal to the standard deviation. The mean width obtained for *K. xylinus* cellulose fibrils is within the range of values (33–39 nm) previously determined from SEM images for BC after 1–3 days of cultivation (Fang and Catchmark 2014; Lee et al. 2015; Martínez-Sanz et al. 2015b). These values include the thickness of a conductive coating layer (about 2–5 nm), which would in our case indicate true mean widths of around 25 and 15 nm for pure BC fibrils from *K. xylinus* and *A. bogorensis*, respectively.

Previously, the range of fibril widths in *A. bogorensis* and *K. xylinus* celluloses were estimated to be about 5–20 nm and 40–100 nm, respectively (Kumagai et al. 2011). However, the width of BC microfibril bundles or ribbons is known to vary between bacterial strains, cultivation conditions and time, as well as

location in the pellicle (Lee et al. 2015). Therefore, direct comparison of values between different studies is not always meaningful. In addition, measuring the BC fibrils' width manually from microscopy images is not straightforward and can be subjective to some systematic error, because many of the fibrils associate with each other and the width of the two-dimensional projection seen in the images may vary along the fibril axis. Here mostly the thinnest, non-aggregated fibrillar units observed in the SEM images were included in the analysis, which also partly explains the lower values of *K. xylinus* cellulose as compared to other analyses.

Transmission electron microscopy results

Representative TEM images of cellulose synthesized by *K. xylinus* and *A. bogorensis* are presented in Fig. 4a and b, respectively. More TEM images can be found in the Electronic supplementary material (Figure S2). The thinnest fibrillar structures detectable in the images, corresponding probably to individual cellulose microfibrils, had widths of 5–7 nm in *K. xylinus* cellulose and 3–5 nm in *A. bogorensis* cellulose. Therefore, a typical 50-nm-wide fibril bundle in *K. xylinus* cellulose consisted of around 6–10 cellulose microfibrils. The *A. bogorensis* cellulose bundles, on the other hand, had fewer microfibrils associated with each other, often only a few but sometimes also around 5 or more. However, one needs to keep in mind that the negative staining and possible effects of drying may affect the detectability and dimensions of the smallest structures in the TEM images.

An analysis of fibril widths in the TEM images (Fig. 4c) yielded mean widths of 53 ± 31 nm and 13 ± 7 nm for *K. xylinus* and *A. bogorensis* celluloses, respectively. The wider distribution of fibril width in *K. xylinus* cellulose is partly explained by a flatter, ribbon-shaped morphology, which was often oriented to the plane of the hydrophilic carbon film on the TEM grid. On the other hand, the smaller number of analyzed images and fibrils together with the

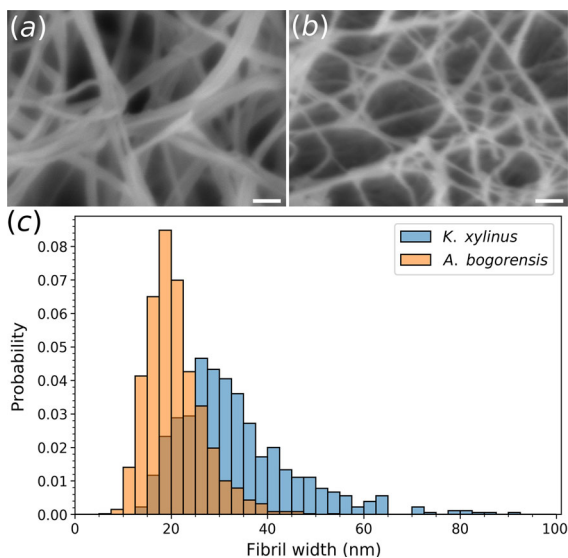


Fig. 3 Example SEM images (scale bar 100 nm) of cellulose produced by **a** *K. xylinus* and **b** *A. bogorensis*; **c** BC fibril width distributions based on SEM images

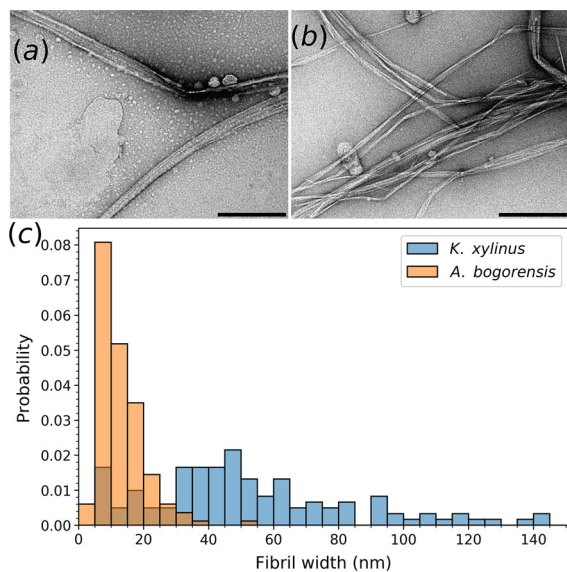


Fig. 4 Example TEM images (scale bar 200 nm) of cellulose produced by **a** *K. xylinus* and **b** *A. bogorensis*; **c** BC fibril width distributions based on TEM images

possibility to detect both microfibril bundles and individual microfibrils explain the polydisperse fibril width distribution of especially *K. xylinus* cellulose and other differences to the analysis based on SEM images (Fig. 3c). It is also possible that the sonication treatment used to disperse the once dried BC fibrils prior to TEM sample preparation could have broken some of the larger microfibril bundles, whereas in the freeze-dried samples imaged with SEM the microfibrils could be strongly aggregated as compared to their original, hydrated structure.

Atomic force microscopy results

Example AFM images of the two BCs and their fibril width distributions are shown in Fig. 5. In both samples the three-dimensional fibril network had collapsed during drying and therefore the images showed a rather flat arrangement of partly overlapping BC fibrils randomly oriented in the plane. In line with the SEM and TEM observations (“[Scanning electron microscopy results](#)” and “[Transmission electron microscopy results](#)” sections), the fibrils synthesized by *A. bogorensis* (Fig. 5c, d) were clearly thinner than those from *K. xylinus* (Fig. 5a, b). An analysis of several AFM images from both samples (Fig. 5e) yielded mean fibril widths of 130 ± 25 nm and

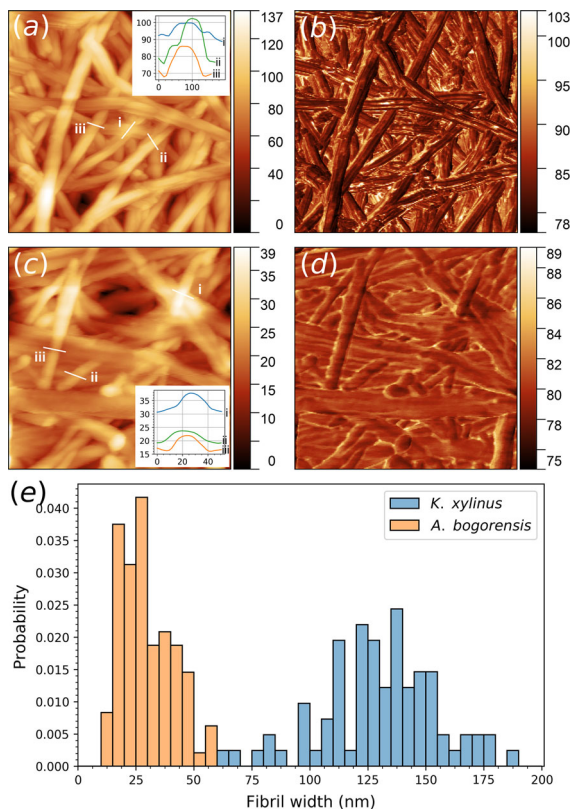


Fig. 5 AFM images of BC samples: **a** topography image (color scale in nm) and **b** phase image (color scale in degrees) of *K. xylinus* cellulose (area $2.0 \mu\text{m} \times 2.0 \mu\text{m}$), **c** topography image and **d** phase image of *A. bogorensis* cellulose (area $0.5 \mu\text{m} \times 0.5 \mu\text{m}$), with example height profiles (units nm) shown in the insets of the topography images; **e** BC fibril width distributions based on AFM amplitude images

30 ± 11 nm for *K. xylinus* and *A. bogorensis* celluloses, respectively. The obtained values confirm the visually observed difference between the two BC samples, even though both of them are larger than the fibril widths determined from the SEM and TEM images. In the AFM images, the fibril width in the plane of the two-dimensional image usually corresponded to the larger dimension of bundle or ribbon cross-section, which together with limited image resolution and possible aggregation while drying explains the different values compared to the SEM and TEM analyses. Previously, fibril widths in the range 110–140 nm were reported from AFM images of *Acetobacter* cellulose samples prepared by drying as a film (Faria Tischer et al. 2010).

The fibril bundles or ribbons of *K. xylinus* cellulose were observed to consist of thinner parallel fibrils,

which were particularly well visible as dark and light stripes along the long axis of some fibrils in the phase images (Fig. 5b). This kind of variation of the phase shift can be associated to differences in sample stiffness (Magonov and Reneker 1997) and could indicate that those bundles or ribbons consisted of harder fibrils (appearing darker) separated by softer interfibrillar spaces (appearing lighter). The typical distance between neighboring stripes was about 10–20 nm, which is two to three times the cross-sectional size of the cellulose crystals based on XRD analysis (Table 1) or the smallest structures observed with TEM (“Transmission electron microscopy results” section). These substructures were not observed in the *A. bogorensis* cellulose (Fig. 5d), which could be due to the limited resolution of the images and effects of tip-broadening.

In addition to the fibril width in the plane of the image, the collapsed morphology of the BC fibril network allowed a rough estimation of the fibril bundle thickness from the AFM topography images. As demonstrated by the example height profiles shown in the insets of Fig. 5a, c, the typical thickness of a BC fibril bundle or ribbon in the out-of-plane direction was around 10 nm in *K. xylinus* cellulose and around or below 5 nm in *A. bogorensis* cellulose, reflecting the same trend as observed in their lateral width. However, a more detailed analysis of the vertical fibril thickness would require a sample with the BC fibrils distributed on a flat surface.

Small-angle scattering results

SAXS and SANS were employed to characterize the hierarchical structure of the two BCs in their original, wet state prior to any drying. The data were fitted with the unified exponential/power-law model (Eq. 2), which allows simultaneous characterization of the hierarchical BC structure on both the levels of single microfibrils and bundles thereof. The SAXS and SANS data with fits are presented in Figs. 6 and 7, respectively, and the most important fitting parameters are summarized in Table 2. A table showing all the fitting parameters (Table S1) and figures presenting the SANS and SAXS data together (Figure S3) are included in the Electronic supplementary material. The SAXS data of *K. xylinus* cellulose (Figure 6a) was fitted only with the terms of the smallest structural level ($i = 1$) and the power-law term of level $i = 2$

(term with B_2 in Eq. 2) due to limited q range. For the same reason, the largest hierarchical level ($i = 3$) was omitted in the SAXS fit to *A. bogorensis* cellulose (Fig. 6b). The SANS data were fitted with the complete expression of Eq. 2 (Fig. 7). A peak between $q = 0.09$ and 0.15 \AA^{-1} in the SANS data of *A. bogorensis* cellulose (Fig. 7b) was excluded from the fit, because with SAXS it was observed only in some parts of the sample and therefore assumed to originate from some unidentified impurities in the larger SANS sample. The value of P_1 was fixed to 4 in all fits.

Estimates for the cross-sectional diameter of BC microfibrils and bundles thereof can be calculated based on the fitting parameters $R_{g,i}$ in Eq. 2. The “cross-sectional radius of gyration” is $R_{g,c} = \sqrt{2/3}R_g$ and by assuming a circular cross-section for simplicity, the cross-sectional diameter of cylindrical fibrils is $D = 2\sqrt{2}R_{g,c}$. The values of D_i for structural levels $i = 1$ and $i = 2$, assumed to correspond to the cross-sectional diameters of BC microfibrils (D_1) and bundles thereof (D_2), are presented in Table 2. The values of D_1 are in good agreement with the cross-sectional dimensions of the BC crystallites determined with XRD (Table 1) as well as the width of the smallest fibrillar structures observed with TEM (“Transmission electron microscopy results” section) and the thickness of fibril bundles determined from the AFM height profiles (“Atomic force microscopy results” section). The relatively large difference between the D_1 values obtained for *A. bogorensis* cellulose based on SAXS and SANS could be due to the removal of data points corresponding to the impurity peak in the SANS data, which particularly affected the intensity at high q values. On the level of the BC microfibril bundles ($i = 2$), the fits to SAXS and SANS data from never-dried samples reproduced the same trend as observed with all other methods: the diameter of the microfibril bundles (D_2) was significantly larger in BC synthesized by *K. xylinus* than by *A. bogorensis*, the ratio between the values from SANS data being about 1.7. The values of the power-law exponents P_2 and P_3 describe the aggregation of the BC microfibrils and their bundles, respectively, and did not show any major difference in the packing of the fibrillar units in the two celluloses.

The main advantages of small-angle scattering methods in BC characterization include the ease of

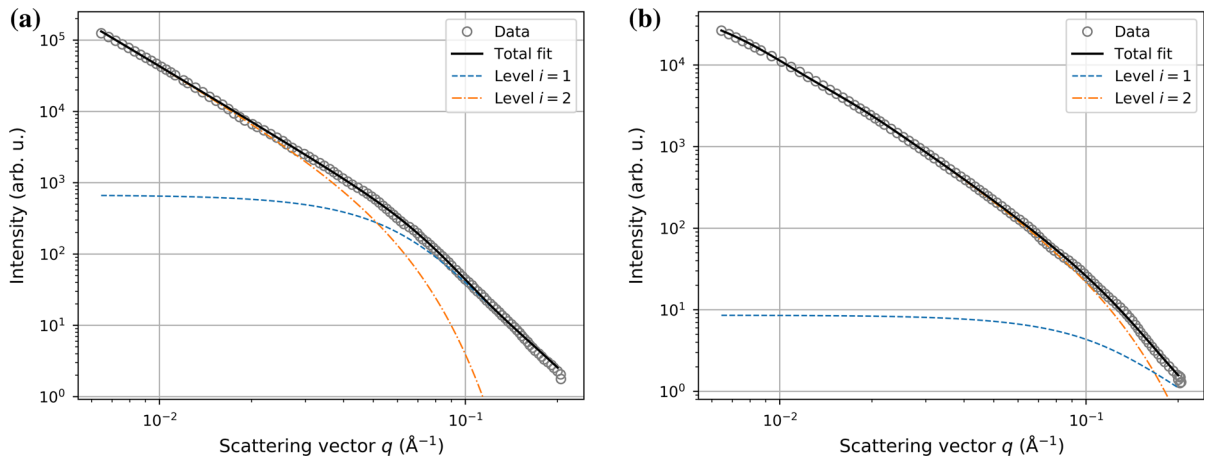


Fig. 6 SAXS data of cellulose produced by **a** *K. xylinus* and **b** *A. bogorensis*, showing the total fit and contributions from the different hierarchical levels

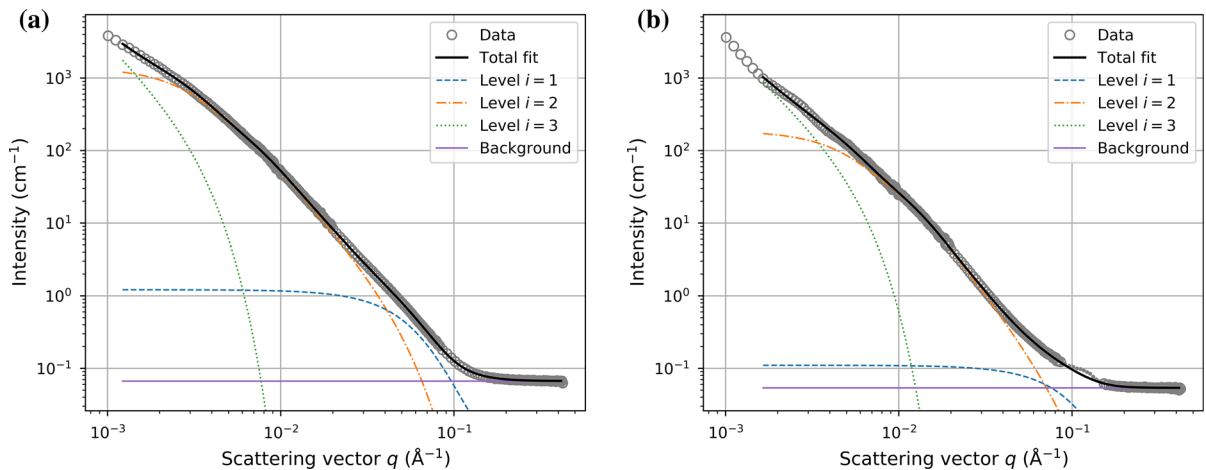


Fig. 7 SANS data of cellulose produced by **a** *K. xylinus* and **b** *A. bogorensis* (peak excluded from the fit denoted by dots), showing the total fit and contributions from the different hierarchical levels

Table 2 Results of fits (Eq. 2) to small-angle scattering data ($R_{g,i}$, P_i) and cross-sectional fibril diameters (D_i) calculated based on $R_{g,i}$. The parameter P_1 was fixed to 4 in all fits

Bacterium	Method	$R_{g,1}$ (nm)	D_1 (nm)	$R_{g,2}$ (nm)	D_2 (nm)	P_2	P_3
<i>K. xylinus</i>	SAXS	3.224(5)	7.45(1)	–	–	2.543(1)	–
	SANS	3.41(1)	7.88(3)	55.3(5)	128(1)	2.688(4)	2.34(2)
<i>A. bogorensis</i>	SAXS	1.445(8)	3.34(2)	26.21(5)	60.5(1)	2.517(1)	–
	SANS	1.94(3)	4.48(7)	32.0(2)	74.0(5)	2.982(5)	2.18(1)

sample preparation, which does not require drying, and the possibility to cover simultaneously two or more levels of the hierarchical structure, depending on

the available q range of the scattering instrumentation. SAXS and SANS can provide the average structure of a macroscopic sample volume, which allows one to

determine the average nanoscale structure more efficiently than with microscopy methods, but at the same time includes a contribution from possible contamination in the sample. The most challenging part of a small-angle scattering experiment is the data analysis, which usually requires fitting of a model function. As has been seen in the literature (Astley et al. 2001; Faria Tischer et al. 2010; He et al. 2014; Martínez-Sanz et al. 2015a, b; Penttilä et al. 2017), the choice of the best model for BC samples is far from well-established and this affects the results. Particularly, the exact shape and size of the BC fibril cross-section is difficult to assess due to the broad size distribution present in native BC. To overcome this challenge in the future, BC with less polydisperse fibril width distribution could be used in order to develop a better analytical model for fitting to small-angle scattering data.

Between the two small-angle scattering methods, SAXS is typically more easily available, has better instrumental resolution, and allows faster measurements from smaller samples than SANS. On the other hand, SANS offers the possibility of contrast variation (Martínez-Sanz et al. 2015a), which can be especially beneficial for studies of multicomponent systems, it does not cause beam damage, and can be used to obtain a more representative picture of a large sample than with SAXS. In a two-component system like in the current case and provided that the q range available with both methods is the same, SAXS and SANS are expected to yield practically the same information. As shown in this work, they can be used to extract the lateral width of BC fibrils both on the level of cellulose microfibrils and their bundles in the original, hydrated state, yielding values that are consistent with each other and comparable with results from other methods. With a proper analytical model developed for BC samples, their potential could be even higher.

Differences between *K. xylinus* and *A. bogorensis* celluloses and their biological origin

BC fibrils consist of thinner sub-fibrils, usually called cellulose microfibrils, that are organized into bundles or larger, ribbon-like structures (Brown 1996; Haigler et al. 1982). The width of the full microfibril bundle varies for instance with cultivation time, which is explained by an increasing number of smaller bundles that become associated with each other (Zhang 2013).

In this mechanism the width of the individual cellulose microfibrils is constant and their number per bundle increases with time. According to the results of this work, however, the cellulose fibrils produced by *A. bogorensis* were thinner than those produced by *K. xylinus* on both hierarchical levels, which cannot be explained solely by a different number of microfibrils forming a bundle or ribbon. Therefore, reasons for the differences should be sought on a more fundamental level of cellulose biosynthesis.

In the molecular scale, the most recent models for the *Acetobacter* cellulose-synthesizing complex (CSC) (Du et al. 2016; Sun et al. 2017) suggest that four cellulose chains, each of them originating from one CesAB complex, pass through the four tunnels of one CesD protein in the periplasmic space (Hu et al. 2010), thereby forming a putative “mini-sheet” (Brown 1996). Even though the structure of the CesD protein is slightly different in *A. bogorensis* (Mizuno & Amano, Bacterial Nanocellulose Conference 2015 abstracts), its octameric shape with a cross-like hole in the middle suggests that also in that case four chains pass through the protein and form the primary assembly of cellulose chains. Therefore, it seems also unlikely that the difference between the microfibril width of *K. xylinus* and *A. bogorensis* celluloses would be merely related to differences in the structure of single CSCs and the proteins constituting them.

Instead, the thinner microfibrils of *A. bogorensis* cellulose are probably explained by a lower number of CSCs that form one subunit of a larger terminal complex (TC). The four-chain subunits or mini-sheets may assemble into microfibrils with cross-sectional dimensions around 5 nm either directly in a single process or through an intermediate phase, such as a “mini-crystal” (Brown 1996; Ross et al. 1991) originating from one TC subunit and having cross-sectional dimensions of 1.5 nm × 1.5 nm (Fig. 8a). Independent of the possible presence of an intermediate structure, the eventual cross-sectional dimensions of the BC microfibrils are likely to be proportional to the number of CSCs or TC subunits contributing to them. Examples of microfibril cross-sections possibly originating from assemblies of 6 and 15 TC subunits are sketched for illustrative purposes in Fig. 8b, c, where the microfibril dimensions roughly correspond to the dimensions determined with XRD and other methods for *A. bogorensis* and *K. xylinus* celluloses, respectively. In further support of TC

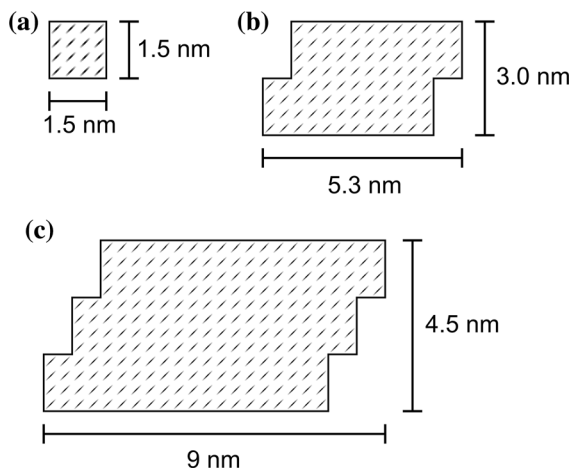


Fig. 8 Schematic cross-sectional views of various arrangements of putative cellulose “mini-crystals”: **a** a single cellulose mini-crystal consisting of 4×4 cellulose chains and synthesized by one TC subunit; possible arrangements of cellulose mini-crystals synthesized by **b** 6 and **c** 15 such TC subunits

subunit numbers close to those presented in Fig. 8b, c, similar ratios around 2 between the two BCs were observed in the crystal size from XRD analysis (Table 1), the microfibril width from SAXS and SANS fits (D_1 in Table 2), and the microfibril bundle thickness from AFM height profiles (“Atomic force microscopy results” section). The similarity of the values from these three methods also implies that drying of the samples prior to the XRD and AFM measurements did not have a significant effect on the thickness of individual BC microfibrils.

Similarly to the BC microfibrils, the ratio of fibril bundle widths between the two BCs was close to 2 when determined from the SEM images of freeze-dried samples (“Scanning electron microscopy results” section) and the small-angle scattering data of wet BCs (“Small-angle scattering results” section). On the other hand, larger ratios of about 4 were obtained based on the TEM (“Transmission electron microscopy results” section) and AFM images (“Atomic force microscopy results” section). This difference might be an effect of the flatter morphology of the *K. xylinus* microfibril bundles, which were also observed to consist of a larger number of microfibrils than the *A. bogorensis* microfibril bundles (TEM results in “Transmission electron microscopy results” section). Moreover, the BC microfibril bundles or ribbons were sensitive to effects of drying, which explains the broader range of values obtained for their

lateral dimensions with the different experimental methods. Drying the samples particularly for TEM and AFM imaging oriented the wider face of flat, ribbon-like bundles to the plane of the image, which made them appear wider than for instance in the SEM images. Distinguishing between the fibril bundle width and thickness was difficult also in the small-angle scattering data, due to which a circular cross-section was assumed in the fits. The bundle widths determined from SEM images were smaller than with SAXS and SANS (D_2 in Table 2), which could be due to shrinkage of the bundles during freeze-drying prior to the SEM imaging. Regardless of any drying-related effects, the lower number of microfibrils constituting a microfibril bundle in *A. bogorensis* cellulose could possibly be related to a less regular assembly of the TC subunits on the cell membrane as compared to the well-organized linear TC of *Acetobacter* (Kimura et al. 2001). However, this remains to be shown in future works.

As a conclusion, we suggest that the overall finer fibrils in *A. bogorensis* cellulose as compared to *K. xylinus* cellulose, observed both in the current work and previously by Kumagai et al. (2011), are caused by the combined effect of two factors: (i) thinner cross-section of individual microfibrils, which are synthesized by a lower number of TC subunits working together; (ii) lower number of microfibrils constituting a microfibril bundle, caused by an irregular assembly of TC subunits on the cell membrane. Developing a way to control these factors separately would lead to a better overall control on cellulose structures synthesized by bacteria and open new ways to tailor them for various applications.

Conclusions

A comprehensive multimethod characterization of two BCs showed that the cellulose fibrils synthesized by a substrain of *A. bogorensis* were finer than those of *K. xylinus* on both the levels of individual cellulose microfibrils and bundles or ribbons thereof. The new results on the *A. bogorensis* fibril dimensions were used to discuss the differences in cellulose biosynthesis between the two bacteria. At the same time, this work demonstrated the challenges of determining the lateral dimensions of highly polydisperse and hierarchically structured BC fibrils, which often lead to

slightly different results depending on the method and sample preparation. From the methods compared in this work, only the small-angle scattering methods SAXS and SANS could be used to determine the lateral width of both the BC microfibrils and the microfibril bundles simultaneously and without drying. By understanding the special characteristics of the various methods and regarding them complementary to each other, a consistent picture of BC structure and its origins may be reached.

Acknowledgments This study was funded by the Japan Society for the Promotion of Science (ID no. P15092), Emil Aaltonen Foundation, and the Core Research for Evolutional Science and Technology (CREST) – Japan Science and Technology Agency (JST) (grant no. JPMJCR13B2). The ILL (proposal no. TEST-2747) and ESRF (final numbers 02-01-882 and 02-01-883) are thanked for providing beamtime. The SEM observations and XRD measurements were done with the courtesy of Prof. Hiroyuki Yano at the Research Institute for Sustainable Humanosphere (RISH), Kyoto University. The TEM observations were carried out with the Analysis and Development system for Advanced Materials (ADAM) of RISH, Kyoto University. The AFM imaging was done at the AFM platform of the PSCM and Alain Panzarella from the ESRF/PSCM is thanked for experimental support. The SAXS experiments were performed on the French CRG beamline D2am at the ESRF and Dr. Isabelle Morfin from CNRS/University of Grenoble Alpes, LIPhy is thanked for providing assistance in using the beamline. This work benefited from the use of the SasView application, originally developed under NSF award DMR-0520547. SasView contains code developed with funding from the European Union's Horizon 2020 research and innovation programme under the SINE2020 project, grant agreement no. 654000.

References

- Ashiotis G, Deschildre A, Nawaz Z, Wright JP, Karkoulis D, Picca FE, Kieffer J (2015) The fast azimuthal integration Python library: pyFAI. *J Appl Crystallogr* 48:510–519. <https://doi.org/10.1107/S1600576715004306>
- Astley OM, Chanliaud E, Donald AM, Gidley MJ (2001) Structure of Acetobacter cellulose composites in the hydrated state. *Int J Biol Macromol* 29:193–202. [https://doi.org/10.1016/S0141-8130\(01\)00167-2](https://doi.org/10.1016/S0141-8130(01)00167-2)
- Atalla RH, Hackney JM, Uhlin I, Thompson NS (1993) Hemicelluloses as structure regulators in the aggregation of native cellulose. *Int J Biol Macromol* 15:109–112. [https://doi.org/10.1016/0141-8130\(93\)90007-9](https://doi.org/10.1016/0141-8130(93)90007-9)
- Beaucage G (1995) Approximations leading to a unified exponential/power-law approach to small-angle scattering. *J Appl Crystallogr* 28:717–728. <https://doi.org/10.1107/S0021889895005292>
- Beaucage G (1996) Small-angle scattering from polymeric mass fractals of arbitrary mass-fractal dimension. *J Appl Crystallogr* 29:134–146. <https://doi.org/10.1107/S0021889895011605>
- Breßler I, Kohlbacher J, Thünemann AF (2015) SASfit: a tool for small-angle scattering data analysis using a library of analytical expressions. *J Appl Crystallogr* 48:1587–1598. <https://doi.org/10.1107/S1600576715016544>
- Brown RM Jr (1996) The biosynthesis of cellulose. *J Macromol Sci, Part A: Pure Appl Chem* 33:1345–1373. <https://doi.org/10.1080/10601329608014912>
- Du J, Vepachedu V, Cho SH, Kumar M, Nixon BT (2016) Structure of the cellulose synthase complex of *Gluconacetobacter hansenii* at 23.4 Å resolution. *PLoS ONE* 11(e0155):886. <https://doi.org/10.1371/journal.pone.0155886>
- Fang L, Catchmark JM (2014) Characterization of water-soluble exopolysaccharides from *Gluconacetobacter xylinus* and their impacts on bacterial cellulose crystallization and ribbon assembly. *Cellulose* 21:3965–3978. <https://doi.org/10.1007/s10570-014-0443-8>
- Faria Tischer PCS, Sierakowski MR, Westfahl H Jr, Tischer CA (2010) Nanostructural reorganization of bacterial cellulose by ultrasonic treatment. *Biomacromol* 11:1217–1224. <https://doi.org/10.1021/bm901383a>
- Haigler CH, White AR, Brown RM Jr, Cooper KM (1982) Alteration of in vivo cellulose ribbon assembly by carboxymethylcellulose and other cellulose derivatives. *J Cell Biol* 94:64–69. <https://doi.org/10.1083/jcb.94.1.64>
- He J, Pingali SV, Chundawat SPS, Pack A, Jones AD, Langan P, Davison BH, Urban V, Evans B, O'Neill H (2014) Controlled incorporation of deuterium into bacterial cellulose. *Cellulose* 21:927–936. <https://doi.org/10.1007/s10570-013-0067-4>
- Hu SQ, Gao YG, Tajima K, Sunagawa N, Zhou Y, Kawano S, Fujiwara T, Yoda T, Shimura D, Satoh Y, Munekata M, Tanaka I, Yao M (2010) Structure of bacterial cellulose synthase subunit D octamer with four inner passageways. *Proc Natl Acad Sci USA* 107:17,957–17,961. <https://doi.org/10.1073/pnas.100601107>
- Iwata T, Indrarti L, Azuma J (1998) Affinity of hemicellulose for cellulose produced by *Acetobacter xylinum*. *Cellulose* 5:215–228. <https://doi.org/10.1023/A:1009237401548>
- Kimura S, Chen HP, Saxena IM, Brown RM Jr, Itoh T (2001) Localization of c-di-GMP-binding protein with the linear terminal complexes of *Acetobacter xylinum*. *J Bacteriol* 183:5668–5674. <https://doi.org/10.1128/JB.183.19.5668-5674.2001>
- Klemm D, Heublein B, Fink HP, Bohn A (2005) Cellulose: fascinating biopolymer and sustainable raw material. *Angew Chem Int Ed* 44:3358–3393. <https://doi.org/10.1002/anie.200460587>
- Knudsen EB, Sørensen HO, Wright JP, Goret G, Kieffer J (2013) FabIO: easy access to two-dimensional X-ray detector images in Python. *J Appl Crystallogr* 46:537–539. <https://doi.org/10.1107/S0021889813000150>
- Kumagai A, Mizuno M, Kato N, Nozaki K, Togawa E, Yamana S, Okuda K, Saxena IM, Amano Y (2011) Ultrafine cellulose fibers produced by *Asaia bogorensis*, an acetic acid bacterium. *Biomacromol* 12:2815–2821. <https://doi.org/10.1021/bm2005615>
- Lee CM, Gu J, Kaffe K, Catchmark JM, Kim SH (2015) Cellulose produced by *Gluconacetobacter xylinus* strains

- ATCC 53524 and ATCC 23768: Pellicle formation, post-synthesis aggregation and fiber density. *Carbohydr Polym* 133:270–276. <https://doi.org/10.1016/j.carbpol.2015.06.091>
- Lin SP, Loira Calvar I, Catchmark JM, Liu JR, Demirci A, Cheng KC (2013) Biosynthesis, production and applications of bacterial cellulose. *Cellulose* 20:2191–2219. <https://doi.org/10.1007/s10570-013-9994-3>
- Magonov SN, Reneker DH (1997) Characterization of polymer surfaces with atomic force microscopy. *Annu Rev Mater Sci* 27:175–222. <https://doi.org/10.1146/annurev.matsci.27.1.175>
- Martínez-Sanz M, Gidley MJ, Gilbert EP (2015a) Application of x-ray and neutron small angle scattering techniques to study the hierarchical structure of plant cell walls: a review. *Carbohydr Polym* 125:120–134. <https://doi.org/10.1016/j.carbpol.2015.02.010>
- Martínez-Sanz M, Lopez-Sanchez P, Gidley MJ, Gilbert EP (2015b) Evidence for differential interaction mechanism of plant cell wall matrix polysaccharides in hierarchically-structured bacterial cellulose. *Cellulose* 22:1541–1563. <https://doi.org/10.1007/s10570-015-0614-2>
- McNamara JT, Morgan JLW, Zimmer J (2015) A molecular description of cellulose biosynthesis. *Annu Rev Biochem* 84:895–921. <https://doi.org/10.1146/annurev-biochem-060614-033930>
- Nishiyama Y, Langan P, Chanzy H (2002) Crystal structure and hydrogen-bonding system in cellulose I β from synchrotron x-ray and neutron fiber diffraction. *J Am Chem Soc* 124:9074–9082. <https://doi.org/10.1021/ja0257319>
- Nishiyama Y, Sugiyama J, Chanzy H, Langan P (2003) Crystal structure and hydrogen bonding system in cellulose I α from synchrotron x-ray and neutron fiber diffraction. *J Am Chem Soc* 125:14300–14306. <https://doi.org/10.1021/ja037055w>
- Penttilä P, Schweins R (2017) SANS characterization of Northern European woods. Institut Laue-Langevin (ILL). <https://doi.org/10.5291/ILL-DATA.TEST-2747>
- Penttilä PA, Imai T, Sugiyama J (2017) Fibrillar assembly of bacterial cellulose in the presence of wood-based hemi-celluloses. *Int J Biol Macromol* 102:111–118. <https://doi.org/10.1016/j.ijbiomac.2017.04.010>
- Ross P, Mayer R, Benziman M (1991) Cellulose biosynthesis and function in bacteria. *Microbiol Rev* 55:35–58
- Schneider CA, Rasband WS, Eliceiri KW (2012) NIH Image to ImageJ: 25 years of image analysis. *Nat Meth* 9:671–675. <https://doi.org/10.1038/nmeth.2089>
- Sugiyama J, Persson J, Chanzy H (1991) Combined infrared and electron diffraction study of the polymorphism of native celluloses. *Macromol* 24:2461–2466. <https://doi.org/10.1021/ma00009a050>
- Sun S, Imai T, Sugiyama J, Kimura S (2017) Cesa protein is included in the terminal complex of *Acetobacter*. *Cellulose* 24:2017–2027. <https://doi.org/10.1007/s10570-017-1237-6>
- Tokoh C, Takabe K, Sugiyama J, Fujita M (2002a) Cellulose synthesized by *Acetobacter xylinum* in the presence of plant cell wall polysaccharides. *Cellulose* 9:65–74. <https://doi.org/10.1023/A:1015827121927>
- Tokoh C, Takabe K, Sugiyama J, Fujita M (2002b) CP/MAS ^{13}C NMR and electron diffraction study of bacterial cellulose structure affected by cell wall polysaccharides. *Cellulose* 9:351–360. <https://doi.org/10.1023/A:1021150520953>
- Zhang K (2013) Illustration of the development of bacterial cellulose bundles/ribbons by *Gluconacetobacter xylinus* via atomic force microscopy. *Appl Microbiol Biotechnol* 97:4353–4359. <https://doi.org/10.1007/s00253-013-4752-x>